

Northumbria Research Link

Citation: Liu, Yuexin, Shen, Dongchen, Tu, Zhengkai, Xing, Lu, Chung, Yongchul G. and Li, Song (2022) Room-temperature hydrogen storage performance of metal-organic framework/graphene oxide composites by molecular simulations. International Journal of Hydrogen Energy, 47 (97). pp. 41055-41068. ISSN 0360-3199

Published by: Elsevier

URL: <https://doi.org/10.1016/j.ijhydene.2022.09.199>
<<https://doi.org/10.1016/j.ijhydene.2022.09.199>>

This version was downloaded from Northumbria Research Link:
<https://nrl.northumbria.ac.uk/id/eprint/50411/>

Northumbria University has developed Northumbria Research Link (NRL) to enable users to access the University's research output. Copyright © and moral rights for items on NRL are retained by the individual author(s) and/or other copyright owners. Single copies of full items can be reproduced, displayed or performed, and given to third parties in any format or medium for personal research or study, educational, or not-for-profit purposes without prior permission or charge, provided the authors, title and full bibliographic details are given, as well as a hyperlink and/or URL to the original metadata page. The content must not be changed in any way. Full items must not be sold commercially in any format or medium without formal permission of the copyright holder. The full policy is available online: <http://nrl.northumbria.ac.uk/policies.html>

This document may differ from the final, published version of the research and has been made available online in accordance with publisher policies. To read and/or cite from the published version of the research, please visit the publisher's website (a subscription may be required.)

Room-Temperature Hydrogen Storage Performance of Metal-Organic Framework/Graphene Oxide Composites by Molecular Simulations

Yuxin Liu,^{a,b} Dongchen Shen,^{a,b} Zhengkai Tu,^a Lu Xing^c Yongchul G. Chung^d, Song Li^{a,b*}

^a *Department of New Energy Science and Engineering, School of Energy and Power Engineering, Huazhong University of Science and Technology, Wuhan, 430074, China*

^b *Shenzhen Research Institute of Huazhong University of Science and Technology, Shenzhen, 518057, China*

^c *Mechanical and Construction Engineering, Northumbria University, Newcastle upon Tyne, NE1 8ST, United Kingdom*

^d *School of Chemical Engineering, Pusan National University, Busan, Geumjeong-gu, Gyeongsangnam-do, Republic of Korea*

*Corresponding author.

E-mail address: songli@hust.edu.cn (Song Li)

Abstract

Metal-organic framework/graphene oxide (MOF/GO) composites have been regarded as potential room-temperature hydrogen storage materials recently. In this work, the influence of MOF structural properties, GO functional group contents and different amounts of doped lithium (Li^+) on hydrogen storage performance of different MOF/GO composites were investigated by grand canonical Monte Carlo (GCMC) simulations. It is found that MOF/GO composites based on small-pore MOFs exhibit enhanced hydrogen storage capacity, whereas MOF/GO based on large-pore MOFs show decreased hydrogen storage capacity, which can be ascribed to the novel pores at MOF/GO interface that favors the enhanced hydrogen storage performance due to the increased pore volume/surface area. By integrating the small-pore MOF-1 with GO, the hydrogen storage capacity was enhanced from 9.88 mg/go up to 11.48 mg/g. However, the interfacial pores are smaller compared with those in large-pore MOFs, resulting in significantly reduced pore volume/surface area as well as hydrogen storage capacities of large-pore MOF/GO composite. Moreover, with the increased contents of hydroxyl, epoxy groups as well as carboxyl group modification, the pore volumes and specific surface areas of MOF/GO are decreased, resulting in reduced hydrogen storage performance. Furthermore, the room-temperature hydrogen storage capacities of Li^+ doped MOF/GO was improved with increased Li^+ at low loading and decrease with the increased Li^+ amounts at high loading. This is due to that the introduced Li^+ effectively increases the accessible hydrogen adsorption sites at low Li^+ loading, which eventually favors the hydrogen adsorption capacity. However, high Li^+ loading causes ion aggregation that reduces the accessible hydrogen adsorption sites, leading to decreased hydrogen storage capacities. MOF-5/GO composites with moderate Li^+ doping achieved the optimum hydrogen storage capacities of approximately 29 mg/g.

Keywords: hydrogen storage, composite, molecular simulation, pore size, Li⁺ doping

1. Introduction

Hydrogen has been regarded as a promising alternative to fossil fuels to reduce greenhouse gas emissions and alleviate climate warming. Due to the low density and flammable nature of hydrogen, efficient and safe hydrogen storage plays an important role in the development of hydrogen energy. Conventional hydrogen storage technologies store hydrogen at high pressure up to 700 bar, which may cause safety issues of hydrogen leakage and explosion [1-4]. Recently, physisorption hydrogen storage has drawn increasing attention as an alternative, by which hydrogen can be stored under cryogenic conditions (such as 77 K) or room temperature (such as 298 K) [5]. Compared with cryogenic hydrogen storage by physisorption that requires a refrigeration system and adds up to system complexity, room-temperature hydrogen storage is more adaptable and promising [6, 7]. Among various hydrogen storage materials, metal-organic frameworks (MOFs) have been regarded as potential candidates for room-temperature hydrogen storage due to their extremely large surface area and pore volume [8-12]. It has been reported that nickel-based Ni₂(*m*-dobdc) exhibited a hydrogen storage capacity of 1.0 wt% at 298 K and 100 bar, which surpasses the compressed storage under the same condition [13]. More recently, Jaramillo et al. [6] reported that the vanadium-based V₂Cl_{2.8}(btdd) exhibited an even higher hydrogen uptake of 1.75 wt% at 298 K and 100 bar. However, the room-temperature hydrogen storage capacities of MOFs are still unsatisfactory for practical applications.

Integration of graphene oxide (GO) [14] with MOFs is one strategy to improve hydrogen storage capacity owing to the increased surface area of MOF/GO composites as well as enhanced interaction strength with hydrogen molecules. Liu et al. [15] prepared the HKUST-1/GO composites and found these composites generally exhibited larger surface areas than parent HKUST-1/GO, leading to enhanced hydrogen adsorption capacities (i.e., 3.58 wt%) compared with HKUST-1 (2.81 wt%) at 77 K, 42 bar. MOF-520/GO composite exhibited a significantly increased hydrogen uptake of 14.6 mmol/g compared with 8.5 mmol/g of MOF-520 due to increased host-hydrogen interaction [16]. Furthermore, it is reported that the increased hydrogen storage capacity (1.8 wt%) of Zr-BDC/GO composite is correlated with increased surface area and strengthened interaction compared with Zr-BDC (1.4 wt%) at 77 K, 1 bar [17]. Moreover, structural properties of MOFs and functional groups of GO also affect hydrogen adsorption performance of MOF/GO composites [18-20]. It has been reported that the growth of MOF crystals with cubic units may proceed more normally upon GO because their metal sites were located in parallel or perpendicular planes, which may lead to well-preserved MOF structures within MOF/GO composites [19]. In addition, it has been reported that increasing epoxy, hydroxyl as well as carboxyl groups on GO leads to strengthened interaction between GO and hydrogen molecules, which may be beneficial for hydrogen adsorption of MOF/GO composite [21]. However, in-depth understanding of the impacts of MOF structural properties and GO functional groups on room-temperature hydrogen storage performance of MOF/GO composites are still elusive.

Li⁺ doping is another strategy to improve the hydrogen adsorption capacity of MOFs by providing strong adsorption sites for hydrogen molecules [22, 23]. Ghoufi et al. [24] reported the increased heat

of adsorption (Q_{st}) of Li^+ doped MIL-101(Cr) from 6.6 kJ/mol to 12 kJ/mol by grand canonical Monte Carlo (GCMC) simulations, leading to the enhanced hydrogen uptake from 9.1 to 10 wt% at 77 K, 100 bar. The enhanced hydrogen adsorption of Li^+ doped MOFs was also confirmed by experimental measurements [25], in which the hydrogen uptakes of MIL-101(Cr) and MIL-53(Al) were increased from 72.5 mg/g and 43.4 mg/g to 79.5 mg/g and 54.1 mg/g at 77 K, 100 bar, and from 5.50 mg/g and 3.63 mg/g to 6.55 mg/g and 4.38 mg/g at 298K, 100 bar after Li^+ doping. Recently, our group [26] synthesized the Li^+ doped MIL-100(Fe)/GO composites with the advantages of GO and Li^+ doping. It was found that the Li^+ doped MIL-100(Fe)/GO exhibited a significantly enhanced hydrogen capacity of 2.02 wt% compared with 0.9 wt% of undoped MIL-100(Fe)/GO and 0.86 wt% of Li^+ doped MIL-100(Fe), which is mainly due to the enhanced accessible adsorption sites provided by Li^+ . Although Li^+ doped MIL-100(Fe)/GO offers a novel prototype for improving hydrogen adsorption, the effects of doping different amounts of Li^+ on other MOF/GO composites remain unknown.

In order to investigate the influence of MOF structural properties and GO functional groups on the room-temperature hydrogen storage capacities, the hydrogen adsorption performance of 54 MOF/GO composites were predicted using GCMC simulations and compared with pristine MOFs. The correlation between MOF structural properties and hydrogen adsorption capacities of MOF/GO composite were analyzed. Furthermore, to offer molecular insights into the effect of Li^+ doping on the hydrogen adsorption performance of MOF/GO composites, varying Li^+ doped MOF/GO models were constructed using molecular dynamic (MD) simulations, the room-temperature hydrogen adsorption capacities of different Li^+ doped MOF/GO models were simulated by GCMC simulations. Based on the above investigations, the relationships between the structure MOF structure properties, GO functional groups, doped Li^+ amounts and hydrogen storage capacities of MOF/GO composites can be extracted, which may guide the design of high-performing MOF/GO composite in future.

2. Molecular simulation

2.1. MOF models

Nine different copper paddlewheel-based MOFs in pcu topology were used to build the MOF/GO composites. Each MOF consists of two types of linkers with the same central backbone but respectively terminated with carboxylate groups ($-\text{COO}-$) and nitrogen atoms ($-\text{N}-$) (Fig. 1a). According to literature [19], the pcu-MOFs are likely to grow normally on GO. Herein, nine MOFs were named as MOF- x ($x = 1, 2, 3, 4, 5, 6, 7, 8, 9$) according to the linker type. Moreover, their structural properties were also obtained. The dominant pore diameters (DPD) of different MOFs were obtained by the Gelb-Gubbins method using RASPA 2.0 package [27-29]. Pore volume (V_P), accessible surface area (S_A) and densities of MOFs were calculated using Zeo++ package [30]. To construct MOF models for MOF/GO composites construction, herein the parallel [001] and [00-1] surfaces of MOFs intersected by the carboxylate linkers were truncated by replacing the carboxylate-terminated linkers with acetates (Fig. S1) according to literature [31]. The details can be found in the Supplementary Information (SI).

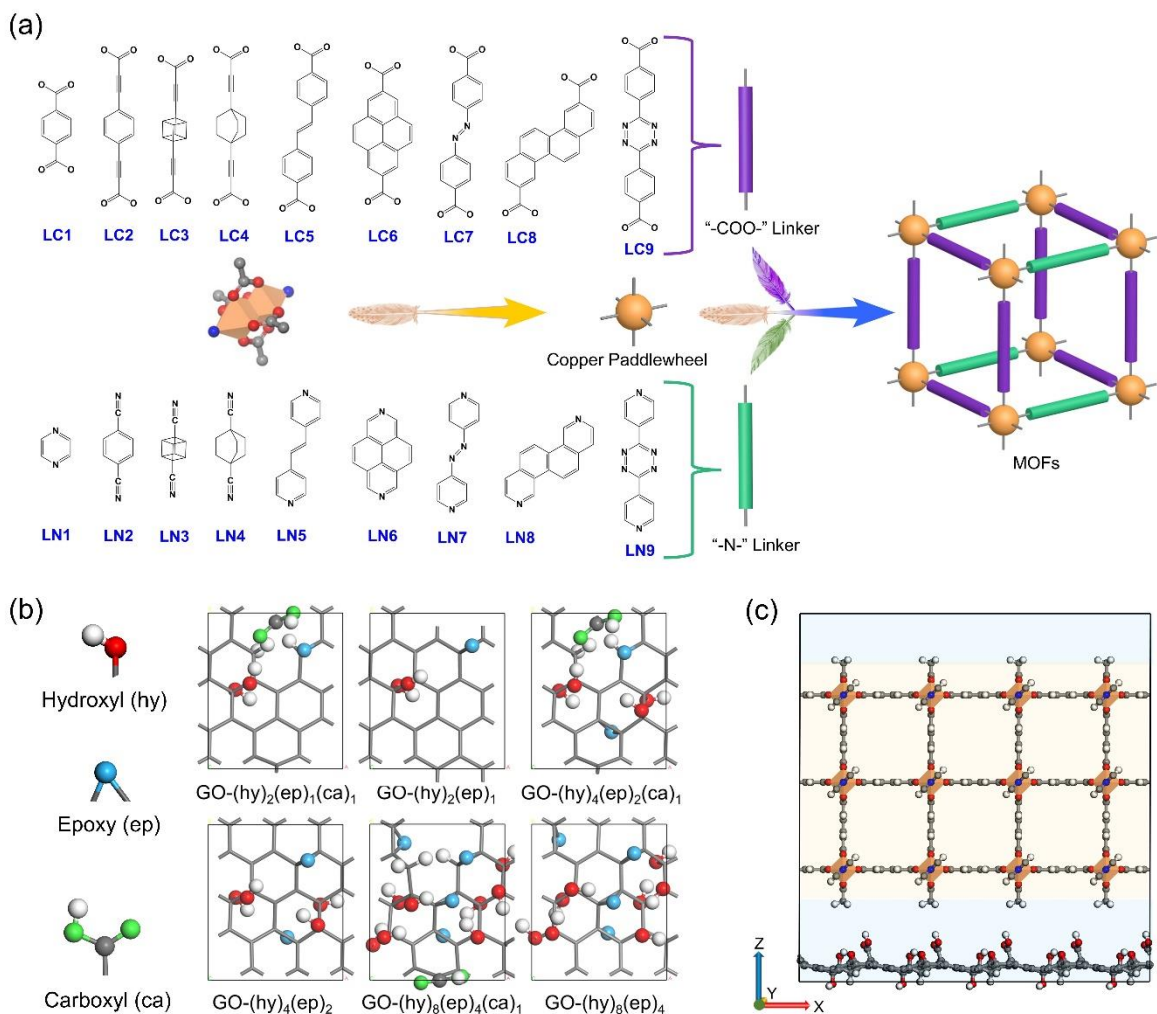


Fig. 1. (a) The schematic structure of nine copper paddlewheel-based MOFs with carboxylate-terminated linkers (“-COO-” linkers) and nitrogen-terminated linkers (“-N-” linkers); (c) Chemical structures of functional groups of GO; (d) Structure of MOF-1-GO-(hy)₂(ep)₁(ca)₁, in which C (grey), H (white), N (blue) and O (red) atoms are depicted by ball-stick models, and the Cu (orange) atoms are depicted by polyhedron models.

2.2. GO models

To build GO models, the pristine graphene unit that consists of 12 carbon rings (Fig. S2) is firstly constructed to fit the geometries of different MOF surfaces (Fig. S3). The pristine graphene unit has a dimension of $7.38 \text{ \AA} \times 8.5216 \text{ \AA}$. According to literature [32], GO generally contains epoxy, hydroxyl and carboxyl groups. Herein, to investigate the influence of increasing epoxy and hydroxyl groups as well as carboxyl modification of GO on the hydrogen storage performance of MOF/GO composites, six different GO unit cells were built based on the pristine graphene unit (Fig. S2), combining three different amounts of epoxy and hydroxyl groups (hydroxyl: epoxy = 2: 1) and two scenarios including one that contains a carboxyl group and another that doesn't contain any carboxyl group (Fig. 1b). The GO unit cells (Fig. 1b) were denoted as GO-(hy)₂(ep)₁(ca)₁, GO-(hy)₂(ep)₁, GO-(hy)₄(ep)₂(ca)₁, GO-(hy)₄(ep)₂, GO-(hy)₈(ep)₄(ca)₁ and GO-(hy)₈(ep)₄, respectively, regarding the number of hydroxyl (hy),

epoxy (ep) and carboxyl (ca) groups. The stable GO structures were obtained using geometry optimization by the DFT method of the DMol3 module of Materials Studio. In the geometry optimization, the GGA-PBE functional was used to calculate exchange-correlation potentials and the Tkatchenko-Scheffler (TS) method was implemented for dispersion correction.

2.3. MOF/GO composite models

The MOF/GO composite models were built as sandwich-like structures and relaxed using geometry optimization by the Forcite module in Materials Studio. Fig. 1c presents the structure of a MOF-1/GO composite as an example, the structures of MOF/GO composites based on other MOFs are shown in Fig. S4. The MOF/GO composites were named as MOF- x -GO-(hy) $_i$ (ep) $_j$ (ca) $_k$ combining the nomenclature of MOFs and GO ($x=1, 2, 3, 4, 5, 6, 7, 8, 9$). Based on the constructed models, the structural properties of the MOF/GO composite were determined. V_P and S_A of the composites were calculated by Zeo++ using the hydrogen probe with a radius of 1.45 Å. Pore size distributions (PSD) of the composites were calculated by the Gelb-Gubbins method using RASPA 2.0 package [27-29]. In Fig. 1c and Fig. S4, the MOF/GO interfaces or interfacial pores are highlighted in blue.

2.4. Li⁺ doped MOF/GO composite models

The Li⁺ doped MOF/GO models were constructed using the molecular dynamic (MD) simulations by the Gromacs package [33], based on the best-performing MOF/GO composites of representative MOFs, namely MOF-1-GO-(hy) $_2$ (ca) $_1$, MOF-3-GO-(hy) $_2$ (ep) $_1$, MOF-5-GO-(hy) $_2$ (ep) $_1$ and MOF-8-GO-(hy) $_2$ (ep) $_1$, which were named as MGO-1, MGO-3, MGO-5 and MGO-8, respectively. To start with, MOF/GO models were filled with water molecules and the water-borne models were then optimized using the MD annealing method to optimize configurations. NVT ensembles were used in the MD annealing processes, in which the temperature, volume and particle number were predetermined. Velocity rescaling method was used to achieve the specified temperature by periodically rescaling the velocities of all particles. Within the MD annealing processes, the system temperature elevated from 298 K to 698 K in 4 ns, remained unchanged in the following 2 ns and then decreased back to 298 K within the next 4 ns, after which the configuration was obtained. Afterwards, different amounts of (i.e., 2, 5, 10, 15, 20, 25, 30) LiCl ion pairs were added to the water-filled MGO models and the same MD annealing processes were used to optimize the distribution of Li⁺ and Cl⁻. Subsequently, the water molecules were gradually removed within five steps to simulate the solvent evaporation processes to obtain the Li⁺ doped MOF/GO models, as shown in Fig. 2. After each step of water molecule removal, a 6 ns MD simulation was performed for equilibration. Noting that Li⁺ doped MOF models were also constructed by similar processes for comparison. For simplicity, Li⁺ doped MOF/GO composites were named as MGO- x - n Li and Li⁺ doped MOFs were named as MOF- x - n Li, with $x=1, 3, 5, 8$ and $n=2, 5, 10, 15, 20, 25, 30$. Settings of MD simulations were presented in the SI. Different from previous studies [23, 34-37] where Li⁺ doped materials were modeled by directly adding only Li⁺ ions to pristine materials followed by optimizations using molecular simulations, solvent evaporation processes were taken into account in this work and the LiCl ion pairs were used in our molecular simulation.

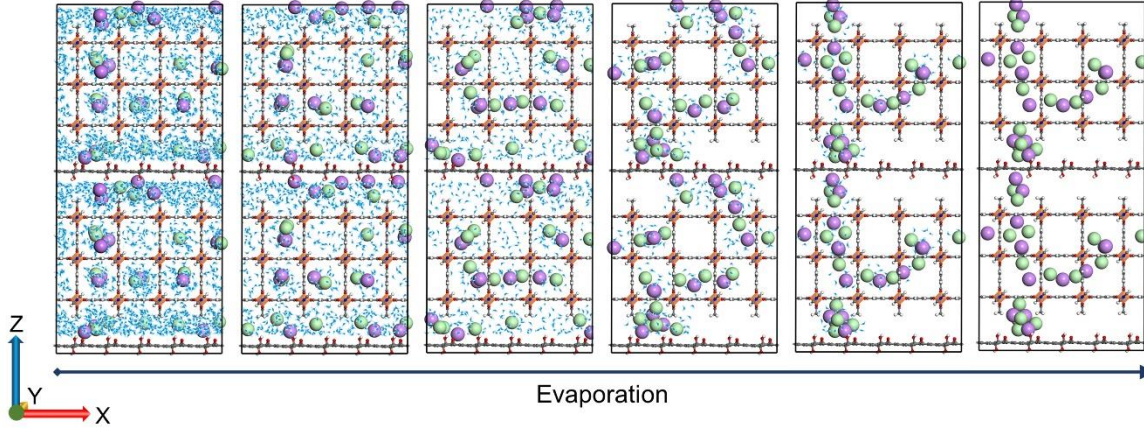


Fig. 2 Simulated evaporation processes of Li^+ doped MOF-1-GO-(hy)₂(ep)₁ model. The $1 \times 2 \times 2$ cells were used to elucidate the distribution of Li^+ within the MOF/GO interface. H (white), C (grey), O (red) and N (blue) atoms of MOF/GO composites are modelled in ball-and-stick models, Cu (orange) atoms are modelled by polyhedron models, Li^+ and Cl^- are depicted by CPK space-filling models [38], water molecules are depicted in line models.

2.5. GCMC simulations

The room-temperature hydrogen adsorption performance was simulated at 298 K by grand canonical Monte Carlo (GCMC) simulations using RASPA 2.0 package [27]. In each GCMC simulation, 3×10^5 GCMC cycles were used for equilibration and another 3×10^5 cycles were used to obtain the statistical ensemble average. The nonbond interaction in Eq. 1 consists of van der Waals interaction as 12-6 Lennard-Jones and electrostatic interaction with the Feynman Hibbs correction included to account for the quantum effect [24].

$$u_{ij} = 4\varepsilon_{ij} \left[\left(\frac{\delta_{ij}}{r_{ij}} \right)^{12} - \left(\frac{\delta_{ij}}{r_{ij}} \right)^6 \right] + \frac{q_i q_j}{4\pi\epsilon_0 r_{ij}} + \frac{\hbar^2}{24\mu_m k_B T} 4\varepsilon_{ij} \left[132 \left(\frac{\delta_{ij}}{r_{ij}} \right)^{12} - 30 \left(\frac{\delta_{ij}}{r_{ij}} \right)^6 \right] \frac{1}{r_{ij}^2} \quad (\text{Eq. 1})$$

The subscript i and j index the different atoms, u_{ij} is the non-bonded potential between atom i and j , ε_{ij} and δ_{ij} are respectively the well depth and equilibrium distance of the 12-6 Lennard-Jones potential, r_{ij} is the distance between atom i and j . q_i and q_j are respectively the charges of atom i and j , ϵ_0 is the vacuum permittivity constant. \hbar is the Planck's constant, μ_m is the reduced mass, k_B is the gas constant and T is the temperature.

Universal forcefield (UFF) for van der Waals interaction and atomic charges calculated using the EEqeq method for the Coulombic interaction were adopted. Parameters of hydrogen molecules models were taken from the Darkrim-Levesque model [39]. In this model, the hydrogen molecule is a rigid, diatomic molecule with H-H bond length fixed at 0.74 Å. The Lennard-Jones parameters (2.958 Å and 36.7 K) are assigned to the center of mass of the hydrogen molecule. Three charges are used in to depict the quadrupole, including two positive charges of $q = 0.468$ e located on the nuclei of each H atom and one negative charge of $q = -0.936$ e located on the center of mass of hydrogen (Fig. S5 and Table S2) [39]. The van der Waals parameters of Li^+ and Cl^- were taken from the literature (Table S1) [24, 26], and the charges of Li^+ and Cl^- are respectively +1 e and -1 e. Van der Waals interaction between

different types of atoms were dominated by Lorentz-Berthelot mixing rule [40, 41]. To investigate the hydrogen distribution within MOF/GO composites and Li⁺ doped MOF/GO, the hydrogen density distributions were also calculated. Besides, potential energy contours of hydrogen adsorption were obtained using the PEGrid package [42].

3. Results and discussion

3.1. Hydrogen adsorption performance of MOF/GO composites

Structural Properties

As shown in Table 1, MOFs exhibit the DPD of 8.4~20.7 Å, V_P of 0.59~3.41 cm³/g, S_A of 2907~6256 m²/g and densities of 0.25~0.83 g/cm³. MOF-1 exhibits the smallest DPD of 8.4 Å, the lowest V_P of 0.59 cm³/g, the lowest S_A of 2907 m²/g and the largest density of 0.83 g/cm³. MOF-9 has the largest DPD and V_P as well as the lowest density, which are 20.7 Å, 3.41 cm³/g and 0.25 g/cm³ respectively. MOF-4 exhibits the largest S_A of 6256 m²/g among nine different MOFs.

Table 1. Structural properties and densities of nine MOFs

MOFs	DPD (Å)	V _P (cm ³ /g)	S _A (m ² /g)	Density (g/cm ³)
MOF-1	8.4	0.59	2907	0.83
MOF-2	15.1	2.68	6149	0.31
MOF-3	13.9	2.24	6062	0.35
MOF-4	14.1	2.09	6256	0.36
MOF-5	16.6	2.80	5515	0.29
MOF-6	12.1	1.44	4410	0.50
MOF-7	16.6	2.69	5378	0.31
MOF-8	13.0	1.57	4673	0.45
MOF-9	20.7	3.41	5396	0.25

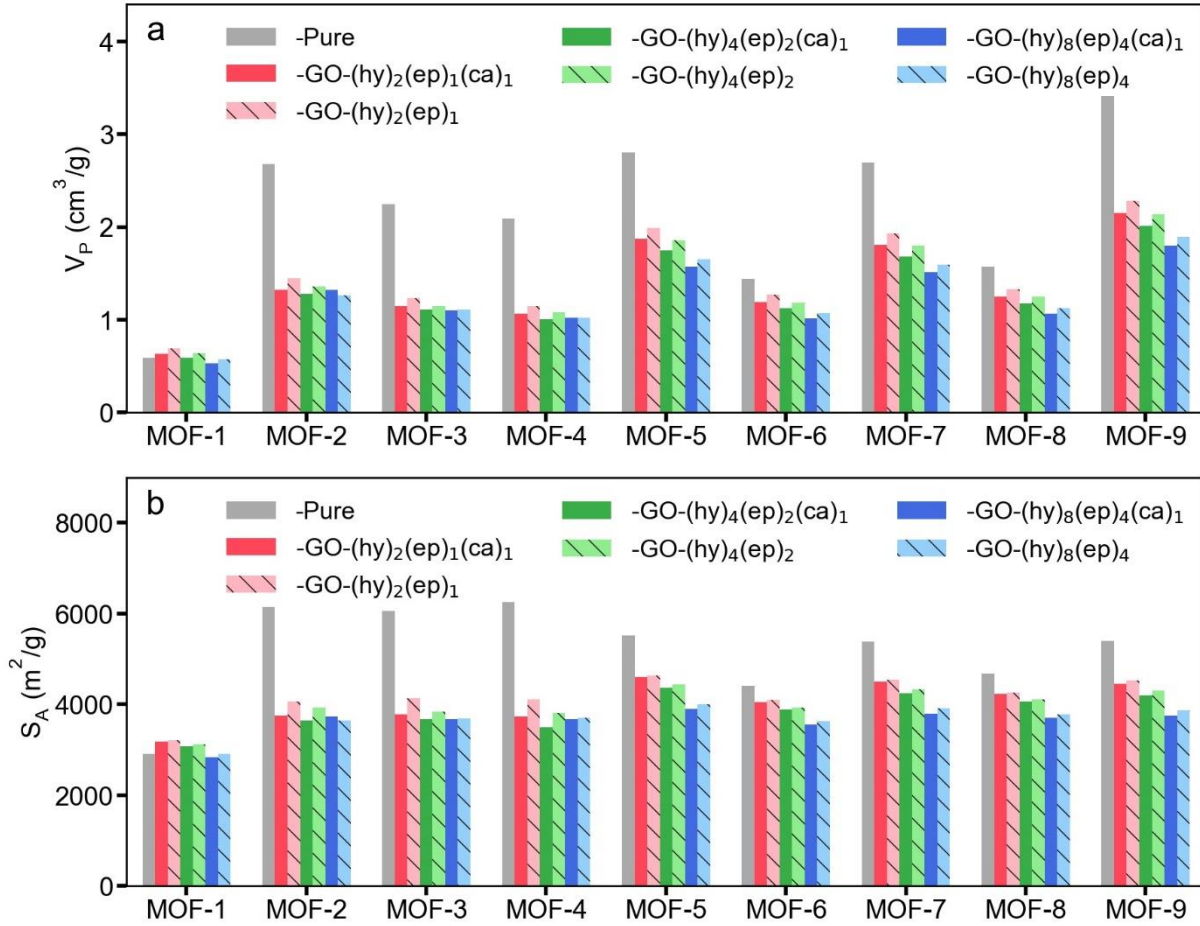


Fig. 3. (a) V_P and (b) S_A of different MOF/GO composites and MOFs

According to literature, room-temperature hydrogen adsorption performance is closely related to the V_P and S_A of adsorbents [43]. As indicated by Fig. 3, for MOF-1 with the lowest DPD (8.4 Å), its MOF/GO composites exhibited enhanced V_P and S_A compared with MOF-1. However, for MOFs with larger DPD (12.1–20.7 Å), GO incorporation led to apparently decreased V_P and S_A . Furthermore, it was found that the V_P and S_A of MOF-3/GO decreased similar to those of MOF-2/GO and MOF-4/GO. V_P and S_A of MOF-5/GO decreased similar to those of MOF-7/GO and MOF-9/GO. V_P and S_A of MOF-6/GO decreased to similar extent with that of MOF-8/GO. Therefore, MOF-3, MOF-5 and MOF-8 were regarded representative among the MOFs with larger pores. Integrated with different functionalized GO, V_P of MOF-3 decreased from 2.24 cm³/g to 1.11~1.23 cm³/g, which decreased by 45%~50%. S_A of MOF-3/GO is decreased from 6062 m²/g to 3671~4145 m²/g. V_P of MOF-5/GO is decreased from 2.80 cm³/g to 1.57~1.99 cm³/g. S_A of MOF-5/GO decreased from 5515 m²/g to 3894~4638 m²/g, which decreased by 16%~29%. V_P of MOF-8/GO decreased from 1.57 cm³/g to 1.06~1.33 cm³/g and its S_A decreased from 4673 m²/g to 3699~4266 m²/g.

According to literature, the formation of novel pores in the MOF/GO interfaces are beneficial for increasing V_P and S_A [15, 19, 26, 44–48]. Liu et al. found that [26] for MIL-100(Fe) with DPD of 9.7 Å/14 Å/26 Å, GO incorporation led to enhanced V_P , mainly due to the increased mesopore (> 20 Å) volumes resulted from the pores formed in the interface between MOF and GO as indicated by the

pore size distributions (PSD). Sun et al. [44] attributed the increased V_P and S_A of MIL-101(Cr)/GO to the interfacial pores. Policicchio et al. [47, 48] indicated that for HKUST-1 with the DPD of 8 Å, GO incorporation led to the formation of new pores of 6 Å/9~10 Å, which contributed to enhanced V_P and S_A . In this work, although interfacial pores were observed in most MOF/GO composites, only the small-pore MOF-1/GO exhibited enhanced V_P and S_A , whereas the MOF/GO with large pores shown decreased V_P and S_A . Based on previous studies, the interfacial pores were generally larger or similar to MOF pores. The V_P and S_A of MOF/GO composites may be related to the relative pore sizes of MOFs and the interfacial pores.

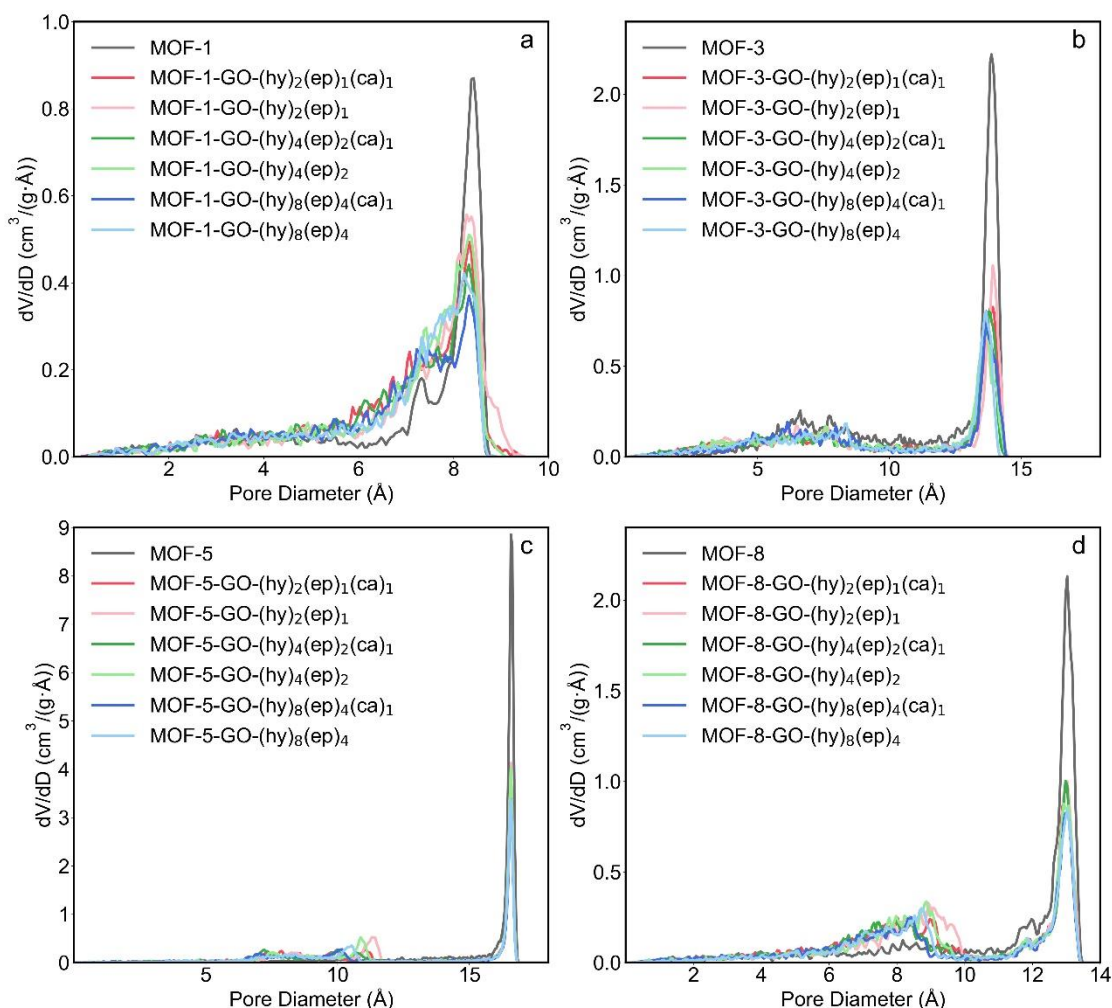


Fig. 4. The pore size distributions (PSD) of MOF/GO composites based on (a) MOF-1, (b) MOF-3, (c) MOF-5 and (d) MOF-8.

To analyze the pore sizes of MOF/GO interface and MOFs, PSD of different MOF/GO composites and MOFs are presented in Fig. 4 and Fig. S6. Results shown that, compared with MOF-1 exhibiting the DPD of 8.4 Å, MOF-1/GO composites exhibited increased pores of 6~8 Å and 8.7~9.5 Å owing to the interfacial pore sizes of around 6-9.5 Å (Fig. 4a). By contrast, the decreased amounts of pores of 8-8.7 Å in MOF-1/GO may be attributed to the decreased proportions of MOF pores due to GO incorporation (Fig. 4a). For MOF-5 with DPD of 16.6 Å, GO incorporation resulted in the formation of MOF/GO interfacial pores of 6-12 Å (Fig. 4c). The MOF-8/GO interfacial pores were 5-10 Å

compared with the DPD (13.0 Å) of MOF-8 (Fig. 4d). Combining V_P , S_A and PSD (Fig. 3 and 4), it was derived that the pores formed in the MOF-1/GO interfaces were similar to MOF-1 pores, which contributed to reduced densities (Fig. S7), resulting in increased V_P and S_A of MOF-1/GO. This mechanism is consistent with the results of abovementioned studies [26, 44, 47, 48]. On the contrary, the other MOF/GO interfacial pores were smaller than the corresponding large-pore MOFs, leading to more compact structures and increased densities (Fig. S7) as well as reduced V_P and S_A .

Besides the DPD of MOFs, the hydroxyl and epoxy groups of GO also affect the structural properties of MOF/GO composites. It was found that MOF/GO composites containing GO-(hy)₂(ep)₁ exhibited the largest V_P and S_A (Fig. 3). V_P and S_A of MOF/GO composites decreased as the contents of hydroxyl and epoxy groups increased, which may be due to that the hydroxyl and epoxy groups occupied additional space in the MOF/GO interfaces (Fig. S7). For example, V_P of MOF-1-GO-(hy)₄(ep)₂ and MOF-1-GO-(hy)₈(ep)₄ were respectively 0.64 cm³/g and 0.57 cm³/g, which were 0.05 cm³/g and 0.12 cm³/g lower than that of MOF-1-GO-(hy)₂(ep)₁, respectively; S_A of MOF-1-GO-(hy)₄(ep)₂ and MOF-1-GO-(hy)₈(ep)₄ were 3124 m²/g and 2097 m²/g, respectively, which were 91 m²/g and 308 m²/g lower compared with that of MOF-1-GO-(hy)₂(ep)₁. Besides, V_P of MOF-5-GO-(hy)₄(ep)₂ and MOF-5-GO-(hy)₈(ep)₄ were reduced by 0.13 cm³/g and 0.34 cm³/g lower, respectively, compared with that of MOF-5-GO-(hy)₂(ep)₁, while the S_A of MOF-5-GO-(hy)₄(ep)₂ and MOF-5-GO-(hy)₈(ep)₄ were reduced by 200 m²/g and 637 m²/g compared with that of MOF-5-GO-(hy)₂(ep)₁, respectively. Similar to the impacts of hydroxyl and epoxy groups, carboxyl group modification also led to reduced void space in the MOF/GO interfaces and increased densities, resulting in decreased V_P and S_A (Fig. 3).

Hydrogen adsorption performance

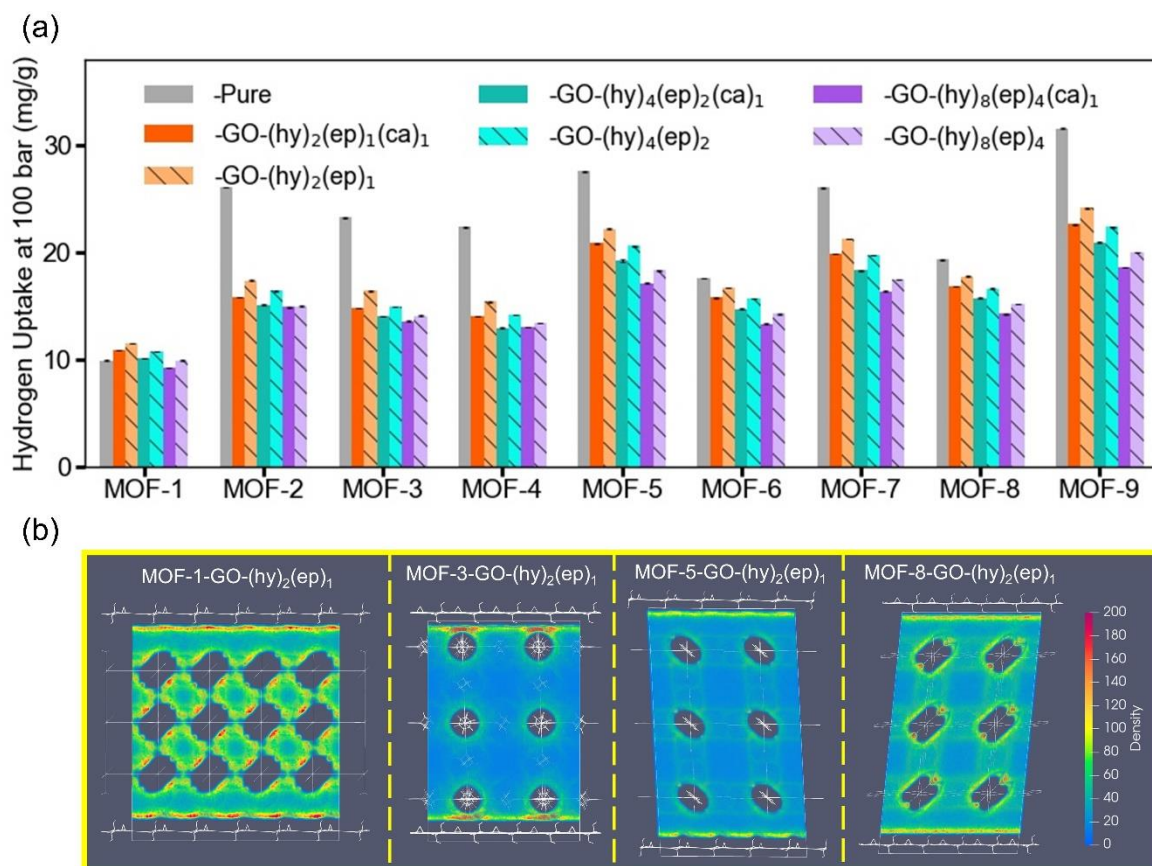


Fig. 5. (a) Hydrogen storage capacities of different MOF/GO composites and MOFs at 298 K, 100 bar. (b) Hydrogen density distribution maps of MOF/GO composites.

Fig. 5a shows the room-temperature hydrogen storage capacities of MOF/GO composites and MOFs. Results shown that small-pore MOF-1 exhibited the lowest hydrogen storage capacity of 9.88 mg/g among nine different MOFs. By integrating MOF-1 with GO, the hydrogen storage capacities were enhanced up to 11.48 mg/g. On the contrary, GO incorporation led to decreased hydrogen storage capacities for large-pore MOFs. The hydrogen storage capacities of MOF-3/GO composites were 13.6~16.4 mg/g, which were 29-42% lower than 23.2 mg/g of MOF-3. Compared with 27.5 mg/g of MOF-5, the hydrogen storage capacities of MOF-5/GO composites decreased to 17.1~22.1 mg/g. The hydrogen storage capacities of MOF-8/GO composites decreased from 19.3 mg/g of MOF-8 to 14.2-17.7 mg/g. To explore the distribution of adsorbed hydrogen molecules in MOF/GO composites, the adsorption density distribution maps of the best-performing MOF/GO composites based on MOF-1, MOF-3, MOF-5 and MOF-8 were analyzed (Fig. 5b). Results shown that the density within the MOF-1 pore is higher than that of larger MOF pores, possibly because the small-pore MOF-1 has stronger interaction with hydrogen compared with large-pore MOFs. Furthermore, though apparent hydrogen density distributions can be observed in the void space of MOF/GO, apparently higher density were observed near the MOF metal clusters and the MOF/GO interfaces, indicating that hydrogen adsorption sites mainly located near metal clusters and MOF/GO interfaces.

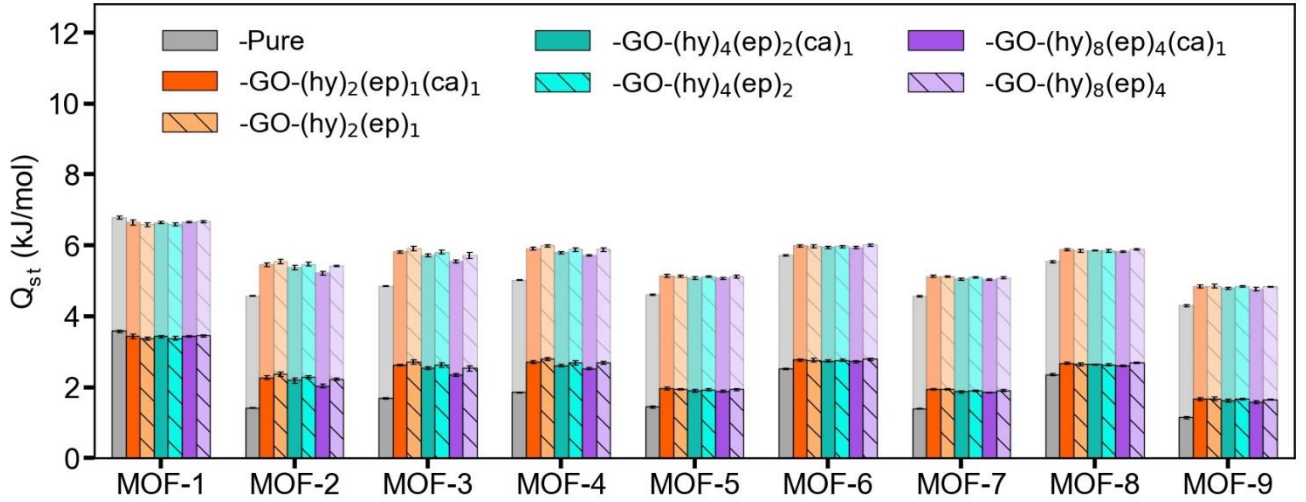


Fig. 6. Heat of adsorption (Q_{st}) of different MOF/GO composites and MOFs, with the contribution of host-adsorbate interaction presented by solid columns highlighted with black edges.

The heat of adsorption (Q_{st}) is calculated to evaluate MOF/GO-hydrogen interaction in Fig. 6. In GCMC simulations, Q_{st} consists of the contributions of host-adsorbate interaction (Q_{st-HA}), the adsorbate-adsorbate interaction (Q_{st-AA}) and a temperature-dependent term (Q_{st-T}), as shown in Eq. 2.

$$Q_{st} = Q_{st-HA} + Q_{st-AA} + Q_{st-T} \quad (\text{Eq. 2})$$

Among the nine MOFs, MOF-1 exhibited the largest Q_{st-HA} (3.6 kJ/mol), which was mainly due to the enhanced potential well overlap within its small pores that led to stronger interaction with hydrogen molecules than the large-pore MOFs. MOF-1/GO composites exhibited slightly decreased Q_{st-HA} than MOF-1, indicating that the interaction between MOF-1/GO and hydrogen is slightly weaker than that between MOF-1 and hydrogen. By contrast, Q_{st-HA} of large-pore MOFs is enhanced by GO incorporation, indicating the strengthened host-adsorbate interaction. By combining Fig. 5b and Fig. 6, it was derived that the enhancement of interaction between large-pore MOF/GO and hydrogen may be attributed to the strong hydrogen adsorption sites within the MOF/GO interfaces. On the contrary, the slightly decreased host-adsorbate interaction of MOF-1/GO may be ascribed to that the interaction between MOF-1/GO interface and hydrogen was slightly weaker than the interaction between MOF-1 and hydrogen due to the potential well overlap of MOF-1, resulting in a decrease in host-adsorbate interaction by GO incorporation.

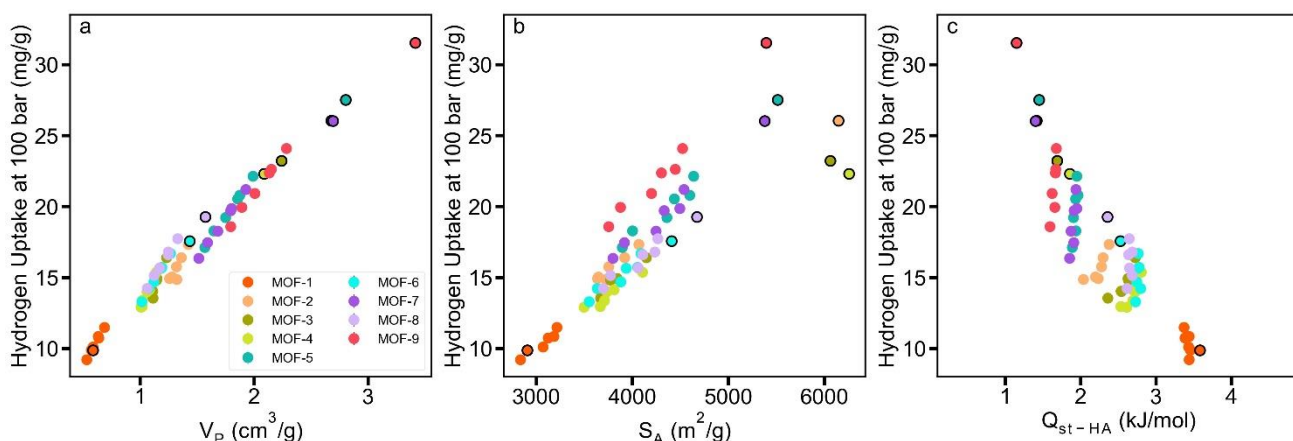


Fig. 7. The correlation between (a) hydrogen storage capacities and V_P ; (b) hydrogen storage capacities and S_A and (c) hydrogen storage capacities and Q_{st-HA} . The data of MOFs are highlighted.

Combining V_P , S_A and Q_{st-HA} (Fig. 3, Fig. 5a and Fig. 6), it was found that the hydrogen storage capacities of MOF/GO composites were positively correlated with the V_P and S_A but inversely related with Q_{st-HA} (Fig. 7). It was derived that, though MOF-1/GO composites exhibited slightly reduced host-adsorbate interaction that was unfavorable for hydrogen adsorption, the enhanced V_P and S_A of MOF-1/GO led to the increased hydrogen adsorption capacities. By contrast, the large-pore MOF/GO composites shown enhanced host-adsorbate interaction that benefits hydrogen adsorption, but their apparently decreased V_P and S_A resulted in decreased storage capacities. According to literature [26], MIL-100(Fe)/GO composites exhibited enhanced hydrogen storage capacities compared with MIL-100(Fe). On the contrary, the large-pore MOF/GO composites shown decreased storage capacities than pristine MOFs, possibly because that the MOFs used in this work are in pcu topology that may incur different MOF-GO interaction compared with MIL-100(Fe) of mtn topology, thus the MOF/GO interfacial pores ($< 15 \text{ \AA}$) of large-pore MOF/GO composites in this work were smaller than the MIL-100(Fe)/GO interfacial pores ($> 20 \text{ \AA}$) and led to apparently reduced V_P , S_A and hydrogen storage capacities.

Regarding the impacts of functional groups of GO on hydrogen storage capacities of MOF/GO composites, the MOF/GO composites based on GO-(hy)₂(ep)₁ exhibited the largest hydrogen storage capacities (by Fig. 5a). The storage capacities based on MOF/GO composites decreased with increased hydroxyl and epoxy groups. More specifically, hydrogen storage capacities of MOF-1-GO-(hy)₄(ep)₂ and MOF-1-GO-(hy)₈(ep)₄ were decreased by 0.73 mg/g and 1.59 mg/g compared with MOF-1-GO-(hy)₂(ep)₁, respectively. While the storage capacities of MOF-5-GO-(hy)₄(ep)₂ and MOF-5-GO-(hy)₈(ep)₄ were reduced by 1.59 mg/g and 3.85 mg/g compared with that of MOF-5-GO-(hy)₂(ep)₁, respectively. Combining V_P , S_A , Q_{st-HA} and hydrogen storage capacities (Fig. 3, Fig. 5a, Fig. 6 and Fig. 7), it was derived that the decreased V_P and S_A were largely accounted for the decreased hydrogen storage capacities considering the interaction between MOF/GO and hydrogen was barely influenced by the increased hydroxyl and epoxy groups (Fig. 6 and Fig. S8). Carboxyl group modification of GO also led to reduced hydrogen storage capacities of MOF/GO composites (Fig. 5a). Since carboxyl

group modification didn't apparently affect the interaction between MOF/GO and hydrogen (Fig. 6), the decreased hydrogen storage capacities were herein attributed to the decreased V_P and S_A (Fig. 3).

3.2. Hydrogen adsorption performance of Li^+ doped MOF/GO

Structural Properties

To further enhance the hydrogen storage capacity of MOF/GO composite, Li^+ doped MOF/GO was investigated. The structure properties of Li^+ doped MOF/GO composites were firstly investigated taking Li^+ doped MGO-1 and MGO-5 for example (Fig. 8). It was revealed that the distributions of Li^+ were related to the types of MOF/GO composites and the amounts of Li^+ . Within the small-pore MGO-1, Li^+ were located within the MOF-1/GO interface at low contents. At high Li^+ loading, Li^+ ions were partially distributed in different MOF-1 pores with the rest aggregating in MOF-1/GO interfaces (Fig. 8a). By contrast, in MOF-1, Li^+ distributed in different MOF-1 pores at varying Li^+ loadings (Fig. 8b). Different from the small-pore MGO-1, Li^+ ions in large-pore MOF/GO composites were mainly located in the MOF/GO interfaces at varying Li^+ loadings, which aggregated at high Li^+ loading (Fig. 8c). By contrast, Li^+ in large-pore MOFs aggregated within MOF pores (Fig. 8d). For both Li^+ doped MOF/GO and Li^+ doped MOFs based on large-pore MOFs, the ions aggregated in a few pores, possibly due to that the dispersed ions in LiCl solutions moved toward each other between different pores in water evaporation processes (Fig. S9). On the contrary, in Li^+ doped MGO-1 and Li^+ doped MOF-1, Li^+ distributed or partially distributed at various MOF-1 pores, possibly because the narrow MOF-1 pores hindered the transportation of ions, thus disfavoring aggregation (Fig. 2).

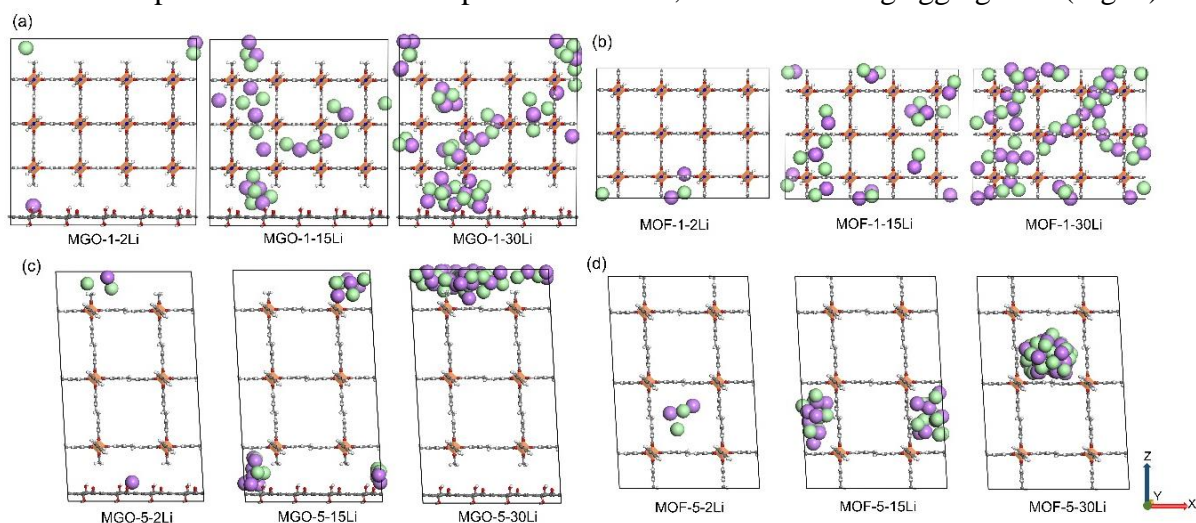


Fig. 8. Li^+ doped (a) MGO-1, (b) MOF-1, (c) MGO-5 and (d) MOF-5. H (white), C (grey), O (red) and N (blue) atoms of MOF/GO composites are modelled in ball-and-stick models, Cu (orange) atoms are modelled by polyhedron models, Li^+ and Cl^- are depicted by CPK space-filling models [38].

Fig. 9 shows the V_P and S_A of different Li^+ doped MOF/GO composites. Li^+ doping led to decreased V_P for MOF/GO composites and V_P of Li^+ doped MOF/GO composites decreased with increased Li^+ loading (Fig. 9a.). By contrast, S_A of Li^+ doped MOF/GO composites is related to their MOF pore sizes (Fig. 9b). For small-pore MGO-1, Li^+ doping led to decreased S_A and the S_A of Li^+ doped MGO-1 decreased with increased Li^+ loading. The S_A of MGO-1 is decreased from 3215 m^2/g to 3211 m^2/g , 3139 m^2/g and 3062 m^2/g by doping 2 Li^+ , 15 Li^+ and 30 Li^+ , respectively. For the large-pore MGO-

3, MGO-5 and MGO-8, doping a small amount of Li^+ led to increased S_A . But the S_A of Li^+ doped MOF/GO composites decreased with increased Li^+ loading. The accessible surfaces of Li^+ doped MOF/GO composites were investigated based on Li^+ doped MGO-1 and Li^+ doped MGO-5 (Fig. S10). For the small-pore MGO-1 (Fig. S10a), the accessible surfaces of the narrow pores were blocked by the added Li^+ and Cl^- after Li^+ doping, and the ion surfaces occluded each other, both of which contributed to decreased S_A (Fig. 9b). Similar mechanism also led to decreased S_A of MOF-1 after Li^+ doping (Fig. 9b and Fig. S10b). By contrast, for the large-pore MOF/GO composites, after doping a small amount of Li^+ , the added ion surfaces were “exposed”, which favors increased accessible surface, leading to increased S_A . However, owing to Li^+ ions aggregation at high loading, the Li^+ ions blocked the pre-existing surfaces (Fig. S10c) and led to decreased S_A (Fig. 9b). Similar mechanism also fits the tendencies of S_A of Li^+ doped MOF-3, MOF-5 and MOF-8 (Fig. 9b and Fig. S10d). Noting that the increased Li^+ also led to decreased pore size distributions of both the MOF pores and MOF/GO interfacial pores (Fig. S11). It should be noted that, regarding Li^+ doping in pcu-MOFs and pcu-MOF/GO, our results (Fig. 8 and Fig. 9) suggest there is probably a limit pore volume of 0.59~0.69 cm^3/g and surface area of 2907~3215 m^2/g for Li^+ aggregation, which requires further investigation.

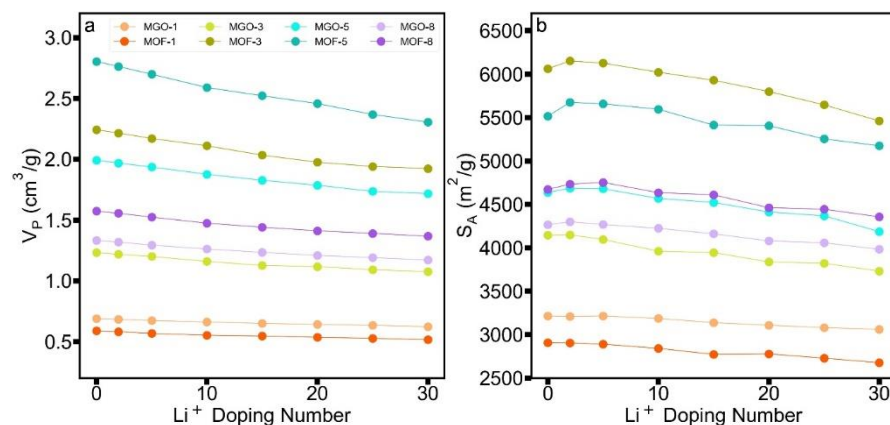


Fig. 9. (a) V_P and (b) S_A of different Li^+ doped materials.

Hydrogen adsorption performance

Room-temperature hydrogen storage capacities of Li^+ doped MOF/GO composites (Fig. 10a) demonstrated that Li^+ doping led to increased hydrogen storage capacities of MOF/GO composites, and the hydrogen storage capacities of Li^+ doped MOF/GO composites were increased with Li^+ loading at lower contents (2-15 Li^+). A moderate loading of Li^+ (15 Li^+) led to the most significant enhancement in storage capacities of MOF/GO composites. Specifically, after doping 2 Li^+ and 15 Li^+ , the storage capacity of MGO-1 was increased from 11.5 mg/g to 11.6 mg/g and 12.1 mg/g, respectively. The storage capacity of MGO-5 was increased from 22.1 mg/g to 22.4 mg/g and 23.1 mg/g, respectively. By contrast, at higher Li^+ loading (15-30 Li^+), the storage capacities of Li^+ doped MOF/GO decreased with Li^+ loading. For instance, after doping 30 Li^+ , the storage capacity of MGO-5 decreased from 22.1 to 21.9 mg/g.

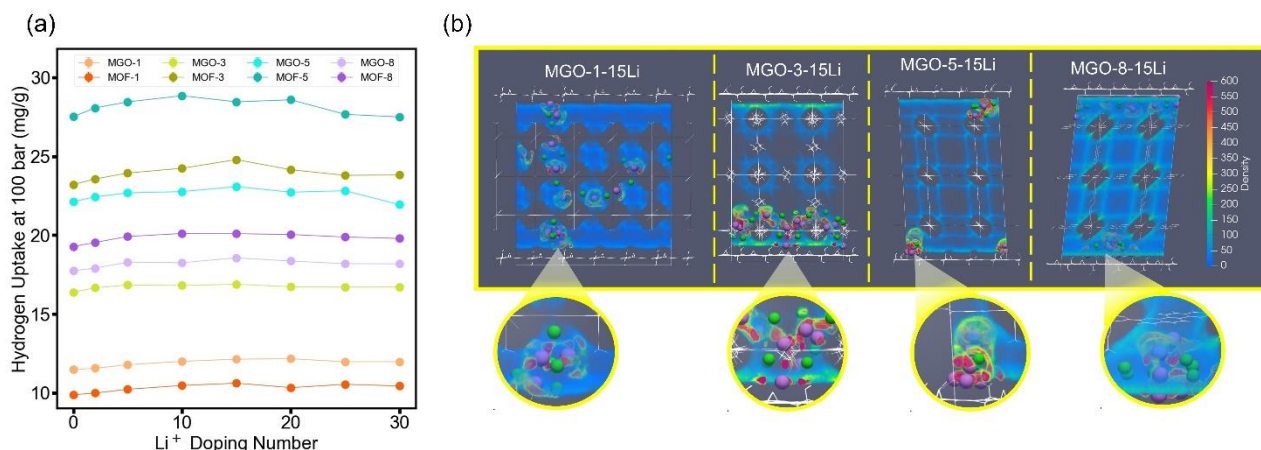


Fig. 10. (a) Room-temperature hydrogen storage capacities of different Li^+ doped MOF/GO composites; (b) Density distribution maps of Li^+ doped MOF/GO composites, taking MGO-1-15Li, MGO-3-15Li, MGO-5-15Li and MGO-8-15Li for example.

The density distribution maps of the 15 Li^+ doped MOF/GO composites (Fig. 10b) revealed that hydrogen density near the Li^+ were apparently higher than that near the metal clusters or within the MOF/GO interfaces, indicating that Li^+ ions provided novel hydrogen adsorption sites, possibly due to the strong affinity of Li^+ ions towards hydrogen molecules. Combining hydrogen storage and density distribution maps (Fig. 10 a and b), it can be derived that the adsorption sites provided by Li^+ may strengthen the interaction between MOF/GO and hydrogen, leading to enhanced hydrogen storage capacities. Furthermore, the increased hydrogen storage capacities at low Li^+ loading and the decreased hydrogen storage capacities at high Li^+ loading may be related to the strengthened interaction towards hydrogen and the decreased V_P and S_A (Fig. 9), which will be discussed later.

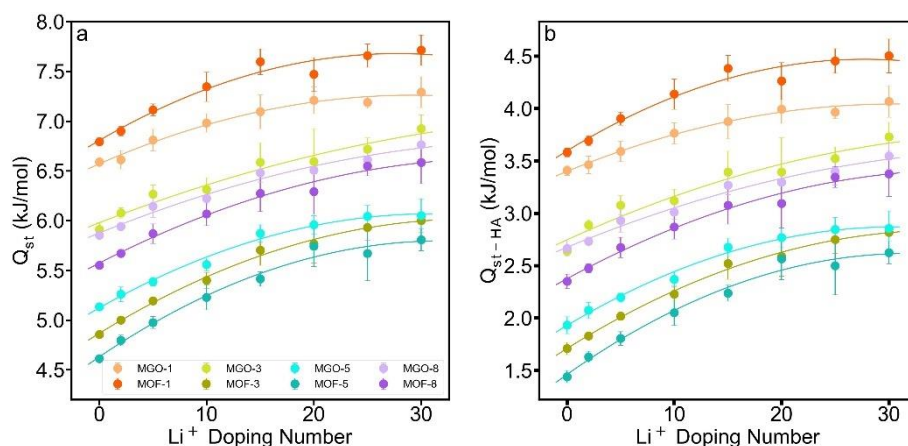


Fig. 11. (a) Heat of adsorption (Q_{st}) and (b) the contribution of host-adsorbate interaction to Q_{st} (Q_{st-HA}) of Li^+ doped materials.

Fig. 11a and b respectively show the heat of hydrogen adsorption (Q_{st}) and the contribution of host-adsorbate interaction to Q_{st} (Q_{st-HA}) of Li^+ doped materials. Results indicated that Li^+ doping led to increased Q_{st-HA} of MOF/GO composites, and the Q_{st-HA} of Li^+ doped MOF/GO composites increased with Li^+ loading, indicating the enhanced host-adsorbate interaction, mainly due to the increased

hydrogen adsorption sites provided by Li^+ . However, it was also indicated that the enhancement in $Q_{\text{st-HA}}$ with Li^+ loading was more remarkable at low loading and less remarkable at high loading. Such a tendency may be attributed to following factors. On the one hand, the Li^+ provides additional hydrogen adsorption sites, contributing to strengthened interaction with hydrogen. On the other hand, as the Li^+ loading increases, ion aggregation reduces adsorption sites provided by Li^+ , metal clusters and MOF/GO interfaces, which offsets the benefits of Li^+ doping (Fig. 8). At low Li^+ loading, the increased Li^+ ions significantly increased the number of adsorption sites, leading to effectively strengthened interaction with hydrogen. By contrast, due to Li^+ ions aggregation at high loading, the number of adsorption sites can be reduced, leading to decreased gains in host-adsorbate interaction (Fig. 11).

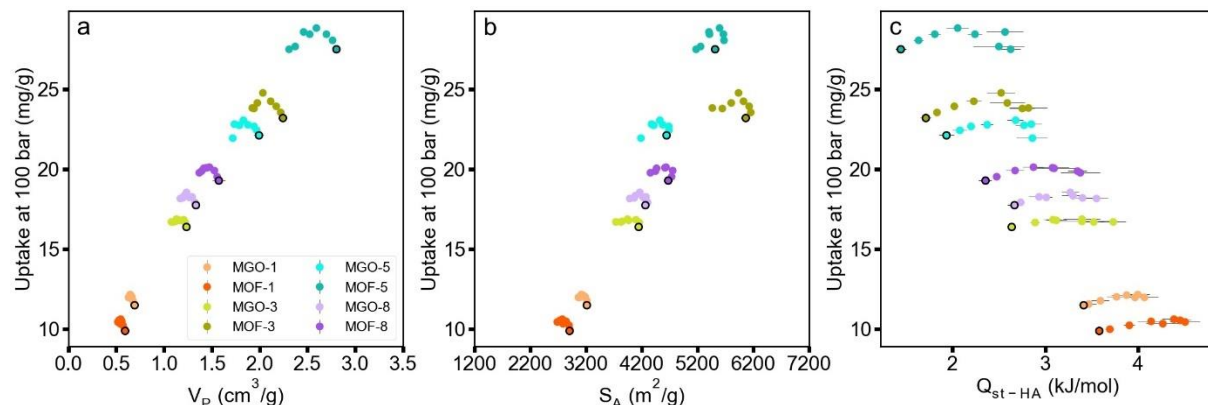


Fig. 12. Correlation between hydrogen storage capacities with (a) V_P , (b) S_A and (c) $Q_{\text{st-HA}}$. The data of undoped MOF/GO composites are highlighted by black edges.

To further elucidate the impacts of Li^+ doping on the hydrogen storage capacities of MOF/GO composites, the correlation between storage capacities and V_P , S_A and $Q_{\text{st-HA}}$ were analyzed (Fig. 12). Li^+ doped MOF/GO, the storage capacities firstly increased and then decreased with V_P , S_A and $Q_{\text{st-HA}}$, concurrently with decreased V_P , S_A and increased $Q_{\text{st-HA}}$ with Li^+ loading (Fig. 9 and Fig. 11). Therefore, the increased storage capacities at low Li^+ loading and the decreased capacity at high loading can be attributed to the following processes. At low Li^+ loading, the added Li^+ effectively increased hydrogen adsorption sites, leading to effectively enhanced host-adsorbate interaction (Fig. 11), resulted in improved storage capacities (Fig. 10a). On the contrary, at high Li^+ loading, the host-adsorbate interaction by introducing Li^+ decreased due to ion aggregation (Fig. 11 and Fig. 8), leading to decreased storage capacities. Noting that similar tendency of storage capacities were observed in Li^+ doped MIL-101(Cr) [25], Li^+ doped fullerene [37], Li^+ doped graphene [36], Li^+ doped MIL-101(Cr)/AC (activated carbon) composites [49] and Li^+ doped MIL-100(Fe)/GO composites [26]. Besides of the harmful influence of ion aggregation as mentioned above, exceedingly Li^+ doping may lead to declined crystallinity and MOF structure deformation of MOF derived materials, which will also deteriorate hydrogen adsorption. Therefore, using a moderate Li^+ amount is crucial for improving Li^+ doped materials. Such conclusions obtained from this work may guide the choosing and designing the high-performing MOF/GO composites with the optimum MOF structure characteristics, GO functional groups and doped Li^+ amounts.

4. Conclusion

In this work, based on 54 MOF/GO composite models, the room-temperature hydrogen storage performance of MOF/GO were systematically investigated by GCMC simulations. It is found that the hydrogen storage performance of MOF/GO composites is related to pore sizes of MOFs. MOF/GO composites based on small-pore MOFs exhibit enhanced hydrogen storage performance, while MOF/GO based on large-pore MOFs show decreased hydrogen storage performance. This is due to the fact that the interfacial pores at MOF/GO interface are close to pores of small-pore MOFs, which contributes to the increased pore volume and specific surface area, leading to enhanced hydrogen storage performance. However, the interfacial pores are smaller than pores of large-pore MOFs, which significantly reduces pore volumes and specific surface areas, thus leading to decreased room-temperature hydrogen storage capacities of MOF/GO composites. Moreover, the room-temperature hydrogen storage capacities of MOF/GO composites are decreased as the contents of functional groups increase, which is ascribed to the fact that these groups reduce pore volumes and specific surface areas, giving rise to decreased hydrogen storage performance. Upon Li^+ doping, the room-temperature hydrogen storage capacities of MOF/GO composites are significantly increased. Which is ascribed to the fact that Li^+ doping provides additional hydrogen adsorption sites that favor the interaction towards hydrogen, leading to enhanced hydrogen storage capacities. Besides, the room-temperature hydrogen storage capacities of Li^+ doped MOF/GO increase with the increase of Li^+ amounts at low loading, and decrease with the increase Li^+ amounts at high loading. This is due to the fact that the introduced Li^+ effectively increases the accessible hydrogen adsorption sites at low Li^+ loading, which eventually favors the hydrogen adsorption capacity. However, at the high Li^+ loading, the accessible hydrogen sites provided by Li^+ decreases due to ion aggregation, leading to decreased storage capacities. Therefore, considering a trade-off between the increased hydrogen adsorption sites resulting from Li^+ doping and the reduced hydrogen adsorption sites resulting from Li^+ aggregation, developing the effective strategies to avoid Li^+ aggregation may be the research focus in future. It should be noted that the synthesizability of these MOF/GO composites is beyond the scope of this work. This work provided molecular insights into the hydrogen storage mechanism of MOF/GO composites, which may guide the design and development of novel hydrogen storage materials.

Acknowledgments

This work was funded by the Basic Research Foundation of Shenzhen (No. JCYJ20190809101403595). We thank the support from Analytical & Testing Center of Huazhong University of Science and Technology.

5. Reference

- [1] Z. Fuquan, M. Zhexuan, H. Han, L. Zongwei. Hydrogen Fuel Cell Vehicle Development in China: An Industry Chain Perspective. *Energy Technology*. 8 (2020).
- [2] Y. Sun, R.F. DeJaco, Z. Li, D. Tang, S. Glante, D.S. Sholl, et al. Fingerprinting diverse nanoporous materials for optimal hydrogen storage conditions using meta-learning. *Science Advances*. 7 (2021) 12.

- [3] H. Barthelemy, M. Weber, F. Barbier. Hydrogen Storage: Recent Improvements and Industrial Perspectives. *International Journal of Hydrogen Energy*. 42 (2017) 7254-62.
- [4] R. Moradi, K.M. Groth. Hydrogen storage and delivery: Review of the state of the art technologies and risk and reliability analysis. *International Journal of Hydrogen Energy*. 44 (2019) 12254-69.
- [5] Z. Ke, Y. Cheng, S. Yang, F. Li, L. Ding. Modification of COF-108 via impregnation/functionalization and Li-doping for hydrogen storage at ambient temperature. *International Journal of Hydrogen Energy*. 42 (2017) 11461-8.
- [6] D.E. Jaramillo, H.Z.H. Jiang, H.A. Evans, R. Chakraborty, H. Furukawa, C.M. Brown, et al. Ambient-Temperature Hydrogen Storage via Vanadium(II)-Dihydrogen Complexation in a Metal-Organic Framework. *Journal of the American Chemical Society*. 143 (2021) 6248-56.
- [7] H. Chen, R.Q. Snurr. Computational Screening of Metal-Catecholate-Functionalized Metal-Organic Frameworks for Room-Temperature Hydrogen Storage. *The Journal of Physical Chemistry C*. 125 (2021) 21701-8.
- [8] Z. Xiang, Z. Hu, D. Cao, W. Yang, J. Lu, B. Han, et al. Metal-organic frameworks with incorporated carbon nanotubes: improving carbon dioxide and methane storage capacities by lithium doping. *Angew Chem Int Ed Engl*. 50 (2011) 491-4.
- [9] H.W. Langmi, J. Ren, B. North, M. Mathe, D. Bessarabov. Hydrogen Storage in Metal-Organic Frameworks: A Review. *Electrochimica Acta*. 128 (2014) 368-92.
- [10] A. Ahmed, S. Seth, J. Purewal, A.G. Wong-Foy, M. Veenstra, A.J. Matzger, et al. Exceptional Hydrogen Storage Achieved by Screening Nearly Half a Million Metal-Organic Frameworks. *Nature Communication*. 10 (2019) 1568.
- [11] H. Zhou, X. Liu, J. Zhang, X. Yan, Y. Liu, A. Yuan. Enhanced room-temperature hydrogen storage capacity in Pt-loaded graphene oxide/HKUST-1 composites. *International Journal of Hydrogen Energy*. 39 (2014) 2160-7.
- [12] H. Zhou, J. Zhang, J. Zhang, X. Yan, X. Shen, A. Yuan. High-capacity room-temperature hydrogen storage of zeolitic imidazolate framework/graphene oxide promoted by platinum metal catalyst. *International Journal of Hydrogen Energy*. 40 (2015) 12275-85.
- [13] M.T. Kapelewski, T. Runcevski, J.D. Tarver, H.Z.H. Jiang, K.E. Hurst, P.A. Parilla, et al. Record High Hydrogen Storage Capacity in the Metal-Organic Framework $\text{Ni}_2(\text{m-dobdc})$ at Near-Ambient Temperatures. *Chemistry of Materials*. 30 (2018) 8179-89.
- [14] X. Huang, X. Qi, F. Boey, H. Zhang. Graphene-based composites. *Chemical Society Reviews*. 41 (2012) 666-86.
- [15] S. Liu, L. Sun, F. Xu, J. Zhang, C. Jiao, F. Li, et al. Nanosized Cu-MOFs Induced by Graphene Oxide and Enhanced Gas Storage Capacity. *Energy & Environmental Science*. 6 (2013) 818.
- [16] B. Szczeńsiak, J. Choma, M. Jaroniec. Development of Activated Graphene-MOF Composites for H_2 and CH_4 Adsorption. *Adsorption*. 25 (2019) 521-8.
- [17] N.M. Musyoka, J. Ren, H.W. Langmi, B.C. North, M. Mathe, D. Bessarabov. Synthesis of rGO/Zr-MOF Composite for Hydrogen Storage Application. *Journal of Alloys and Compounds*. 724 (2017) 450-5.
- [18] B. Szczeńsiak, J. Choma, M. Jaroniec. Gas Adsorption Properties of Hybrid Graphene-MOF Materials. *Journal of Colloid and Interface Science*. 514 (2018) 801-13.
- [19] C. Petit, T.J. Bandoz. Engineering the Surface of a New Class of Adsorbents: Metal-Organic

- Framework/Graphite Oxide Composites. *Journal of Colloid and Interface Science*. 447 (2015) 139-51.
- [20] S. Bashkova, T.J. Bandoz. Insight into the role of the oxidized graphite precursor on the properties of copper-based MOF/graphite oxide composites. *Microporous and Mesoporous Materials*. 179 (2013) 205-11.
- [21] D. Luo, X. Zhang. The Effect of Oxygen-Containing Functional Groups on the H₂ Adsorption of Graphene-based Nanomaterials: Experiment and Theory. *International Journal of Hydrogen Energy*. 43 (2018) 5668-79.
- [22] T.A. Maark, S. Pal. A model study of effect of M = Li⁺, Na⁺, Be²⁺, Mg²⁺, and Al³⁺ ion decoration on hydrogen adsorption of metal-organic framework-5. *International Journal of Hydrogen Energy*. 35 (2010) 12846-57.
- [23] L. Xia, Z. Bo, Q. Liu, X. Zhang, Y. Pei. Li-doped and Functionalized Metal-Organic Framework-519 for Enhancing Hydrogen Storage: A Computational Study. *Computational Materials Science*. 166 (2019) 179-86.
- [24] A. Ghoufi, J. Deschamps, G. Maurin. Theoretical Hydrogen Cryostorage in Doped MIL-101(Cr) Metal-Organic Frameworks. *The Journal of Physical Chemistry C*. 116 (2012) 10504-9.
- [25] P.K. Prabhakaran, J. Deschamps. Hydrogen Adsorption in Lithium Doped MIL-101 and MIL-53(Al) at 77 and 298 K up to 100 bar: Effect of Lithium Concentration. *Journal of Porous Materials*. 22 (2015) 1073-81.
- [26] C. Liu, D. Shen, Z. Tu, S. Li. Improved Room-Temperature Hydrogen Storage Performance of Lithium-Doped MIL-100(Fe)/Graphene Oxide (GO) Composite. *International Journal of Hydrogen Energy*. 47 (2022) 5393-402.
- [27] D. Dubbeldam, S. Calero, D.E. Ellis, R.Q. Snurr. RASPA: Molecular Simulation Software for Adsorption and Diffusion in Flexible Nanoporous Materials. *Molecular Simulation*. 42 (2015) 81-101.
- [28] L. Sarkisov, A. Harrison. Computational Structure Characterisation Tools in Application to Ordered and Disordered Porous Materials. *Molecular Simulation*. 37 (2011) 1248-57.
- [29] L.D. Gelb, K.E. Gubbins. Pore Size Distributions in Porous Glasses: A Computer Simulation Study. *Langmuir*. 15 (1999) 305-8.
- [30] T.F. Willems, C.H. Rycroft, M. Kazi, J.C. Meza, M. Haranczyk. Algorithms and Tools for High-Throughput Geometry-based Analysis of Crystalline Porous Materials. *Microporous and Mesoporous Materials*. 149 (2012) 134-41.
- [31] S. Amirjalayer, M. Tafipolsky, R. Schmid. Surface Termination of the Metal-Organic Framework HKUST-1: A Theoretical Investigation. *The Journal of Physical Chemistry Letter*. 5 (2014) 3206-10.
- [32] J. Zhao, L. Liu, F. Li. *Graphene Oxide: Physics and Applications*. Springer 2015.
- [33] D. Van Der Spoel, E. Lindahl, B. Hess, G. Groenhof, A.E. Mark, H.J. Berendsen. GROMACS: Fast, Flexible, and Free. *Journal of Computational Chemistry*. 26 (2005) 1701-18.
- [34] C. Baykasoglu, Z. Ozturk, M. Kirca, A.T. Celebi, A. Mugan, A.C. To. Effects of lithium doping on hydrogen storage properties of heat welded random CNT network structures. *International Journal of Hydrogen Energy*. 41 (2016) 8246-55.
- [35] M.I. Khan, S.M. Zaigam, A. Majid, M.B. Tahir. Computational insights of alkali metal (Li / Na / K) atom decorated buckled bismuthene for hydrogen storage. *International Journal of Hydrogen Energy*. 46 (2021) 28700-8.
- [36] Z. Öztürk. Lithium Decoration Characteristics for Hydrogen Storage Enhancement in Novel

- Periodic Porous Graphene Frameworks. *International Journal of Hydrogen Energy*. 46 (2021) 11804-14.
- [37] C.U. Deniz, H. Mert, C. Baykasoglu. Li-doped Fullerene Pillared Graphene Nanocomposites for Enhancing Hydrogen Storage: A Computational Study. *Computational Materials Science*. 186 (2021) 110023.
- [38] R.B. Corey, L. Pauling. Molecular Models of Amino Acids, Peptides, and Proteins. *Review of Scientific Instruments*. 24 (1953) 621-7.
- [39] F. Darkrim, D. Levesque. Monte Carlo Simulations of Hydrogen Adsorption in Single-Walled Carbon Nanotubes. *The Journal of Chemical Physics*. 109 (1998) 4981-4.
- [40] H.A. Lorentz. Ueber die Anwendung des Satzes Vom Virial in der Kinetischen Theorie der Gase. *Annalen der Physik*. 248 (1881) 127-36.
- [41] J. Delhommelle, P. Millié. Inadequacy of the Lorentz-Berthelot Combining Rules for Accurate Predictions of Equilibrium Properties by Molecular Simulation. *Molecular Physics*. 99 (2001) 619-25.
- [42] PEGrid. <https://github.com/michelleliu/PEGrid>. 2015. (accessed 30 December 2020)
- [43] H. Frost, R.Q. Snurr. Design requirements for metal-organic frameworks as hydrogen storage materials. *The Journal of Physical Chemistry C*. 111 (2007) 18794-803.
- [44] X. Sun, Q. Xia, Z. Zhao, Y. Li, Z. Li. Synthesis and Adsorption Performance of MIL-101(Cr)/Graphite Oxide Composites with High Capacities of n-hexane. *Chemical Engineering Journal*. 239 (2014) 226-32.
- [45] C. Petit, J. Burrell, T.J. Bandosz. The Synthesis and Characterization of Copper-based Metal–Organic Framework/Graphite Oxide Composites. *Carbon*. 49 (2011) 563-72.
- [46] W. Ren, X. Zhuang, Z. Liu, S. Li. Hydrogen Adsorption Performance of Cu-BTC/Graphene Aerogel Composite: A Combined Experimental and Computational Study. *International Journal of Hydrogen Energy*. 46 (2021) 13097-105.
- [47] A. Policicchio, Y. Zhao, Q. Zhong, R.G. Agostino, T.J. Bandosz. Cu-BTC/Aminated Graphite Oxide Composites as High-Efficiency CO₂ Capture Media. *ACS Applied Material Interfaces*. 6 (2014) 101-8.
- [48] Y. Zhao, M. Seredych, Q. Zhong, T.J. Bandosz. Aminated Graphite Oxides and Their Composites with Copper-based Metal–Organic Framework: in Search for Efficient Media for CO₂ Sequestration. *RSC Advances*. 3 (2013) 9932.
- [49] P.K. Prabhakaran, J. Deschamps. Doping Activated Carbon Incorporated Composite MIL-101 Using Lithium: Impact on Hydrogen Uptake. *Journal of Materials Chemistry A*. 3 (2015) 7014-21.